Supplement of Atmos. Chem. Phys., 25, 18617–18637, 2025
https://doi.org/10.5194/acp-25-18617-2025-supplement

Atmospheric Chemistry and Physics
Open Access
EGU

Supplement of

An updated microphysical model for particle activation in contrails: the role of volatile plume particles

Joel Ponsonby et al.

Correspondence to: Marc E. J. Stettler (m.stettler@imperial.ac.uk)

Contents

S1 Homogeneous ice nucleation and κ-Köhler theory

To estimate the homogeneous ice nucleation temperature for supercooled aqueous solution droplets, we employ a similar approach to the original K15 model. This method provides an estimate for the homogeneous temperature of pure water droplets i.e., those forming from wholly insoluble particles $\kappa = 0$. Here, we extend this analysis to include particles that are not wholly insoluble ($\kappa \neq 0$), where the activity of the surrounding solution depends implicitly on the ambient conditions through the wet particle diameter, $d_w = d_w(S_v, T)$ and explicitly on the particle properties, d_d and κ, as described in Sect. 2.2 of the main text. Regardless, homogeneous ice nucleation is governed by the central expression

$$j = J \cdot V_w, \tag{S1}$$

where j is the freezing rate (ice nucleation events per second), which is given as a product of the freezing rate coefficient J (ice nucleation events per unit volume per unit time) and the liquid water volume, $V_w = \frac{4}{3}\pi(r^3 - r_d^3)$. Assuming that a droplet entirely freezes when an ice nucleation event occurs within its volume, j is constrained as the number of droplets freezing per unit time. Previous studies have demonstrated that for typical cloud droplets with diameters of ~μm and homogeneous ice nucleation temperatures of ~235 K, ln(J) scales inversely proportional to temperature (Murray et al., 2010). If we consider a number of identical droplets within a cooling contrail, while plume temperatures are above the common homogeneous ice nucleation temperature ($T > T_{hom}$), although V_w is maximised, j is limited by small J. As the contrail cools and transitions towards T_{hom}, high plume cooling rates (< -10 K/s) lead to a sharp increase in J, maximising j. During the ice nucleation event, V_w is quickly depleted, and j returns to 0. Incidentally, if the droplet size distribution is monomodal, it is typically narrow enough to conform to the same narrative. Based on this semi-quantitative analysis, it is appropriate to assume a pulse-like nature of j and characterise the freezing event by defining a characteristic freezing timescale,

$$\tau_{frz}^{-1} = \frac{\partial \ln(j)}{\partial t} \approx \frac{\partial \ln(J)}{\partial T}\frac{dT}{dt}, \tag{S2}$$

where we have assumed that changes in ln(V_w) are much slower than changes in ln(J). Using Eq. (S2), we can transform Eq. (S1) to estimate the frozen droplet fraction λ (Murray et al., 2012).

$$\lambda = 1 - e^{-J\tau_{frz}V_w}. \tag{S3}$$

For the below analysis, we choose $\lambda = 1 - \delta$ ($\delta = 10^{-20} \sim 0$) in line with previous studies (Kärcher et al., 2015; Lewellen, 2020) and evaluate τ_{frz}^{-1} according to Eq. (S2). We use the freezing rate coefficient described by Koop et al. (2000), which depends *inter alia* on the activity of the solution, $J = J(a_w)$. For a given particle type defined by d_d and κ and at a given temperature, T, first we evaluate d_w and S_v for saturation ratios $S_v < S_{v,c}$. Next, we evaluate $J = J(S_v, T)$ according to the relations outlined in Koop et al. (2000) using an internal droplet pressure (P) parameterization (Marcolli, 2020). This enables us to evaluate $P = P(S_v, T)$ for saturation ratios $S_v < S_{v,c}$. We can then finally determine the critical saturation

ratio, $S_{v,hom}$ at which we satisfy our predefined threshold, $\lambda \sim 1$. This critical saturation ratio represents approximate conditions for homogeneous ice nucleation within the given particle mode.

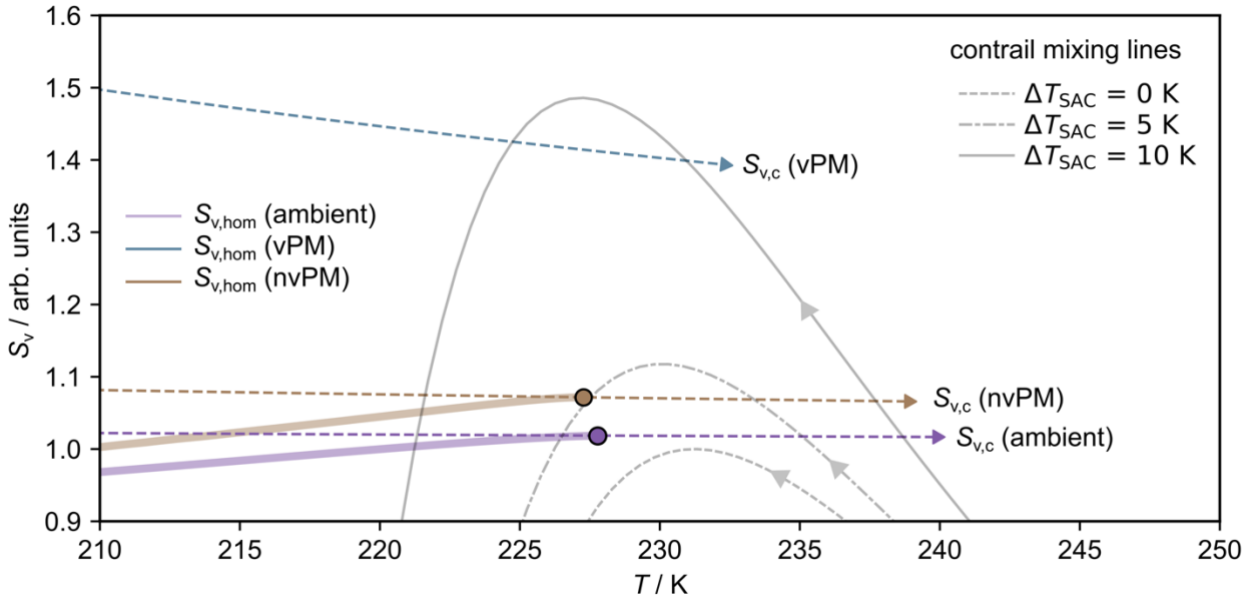

Figure S1: illustrative ice nucleation temperature as predicted using *J* parametrizations from Koop et al. (2000) using the methodology outlined in Kärcher et al. (2015). Particle properties have been taken from Table. 1 in the main text, assuming a sulphur-rich (κ = 0.5) vPM mode with $d_{g,vPM}$ = 4 nm. Several contrail mixing lines have also been presented with G = 1.64.

In Fig. S1, we show the critical saturation ratios required from particle activation and homogeneous ice nucleation, $S_{v,c}$ and $S_{v,hom}$ respectively, for the three particle modes outlined in Table. 1 of the main text for a sulphur-rich vPM mode. The paths traced by $S_{v,hom} = S_{v,hom}(T)$ are also commonly known as "Koop line" freezing thresholds as described by Koop et al. (2000) and in other literature (Baumgartner et al., 2022). For a given particle type, if the ambient conditions lie in the region above the relevant Koop line, the solution droplets are able to freeze homogeneously. The Koop line termini are indicated using coloured markers on Fig. S1, these identify the temperatures beyond which the condition on λ is no longer achieved; for temperatures below the termini, $S_{v,hom}$ asymptotically approaches $S_{v,c}$.We have also shown three contrail mixing lines at three different ambient temperatures corresponding to ΔT_{SAC} of 0 K, 5 K and 10 K. Fig. S1 enables us to determine, for a given particle type, whether particle activation or homogeneous ice nucleation is likely to occur first during the contrail mixing process. We find that for the nvPM and vPM modes (brown and blue lines, respectively), every feasible contrail mixing line first surpasses the critical saturation ratio for droplet activation (bisects $S_{v,c}$) before entering the region above the relevant Koop line. For that reason, we conclude that for the majority of vPM and nvPM particles, droplet activation takes place *prior* to homogeneous ice nucleation. The same conclusion is met for the hygroscopic ambient mode, however for small $\Delta T_{SAC} \sim 0.1$ K, it is possible that a small fraction of the larger particles may freeze homogeneously before they are considered activated. In conclusion, we find that for the three types of particles investigated within this work, we are justified in assuming that particle activation occurs prior to homogeneous ice nucleation.

S2 Radial growth equation

The growth or evaporation of droplets by diffusion of water vapour is described by the radial growth law which may be expressed in the general form (Seinfeld and Pandis, 2016)

$$\frac{dr}{dt} = \frac{G}{r}(S_{\mathrm{e}} - S_{\mathrm{v}}) \,, \tag{S4}$$

where S_{e} is the ambient (environmental) saturation ratio, S_{v} is the equilibrium water saturation ratio above the particle (see Sect. 2.2 of the main text) and G is a growth coefficient. The growth coefficient may be expressed as the sum of two terms, the first of which is associated with heat conduction and the second is associated with water vapour diffusivity (Rogers and Yau, 1996)

$$G = \frac{1}{F_{\mathrm{k}}+F_{\mathrm{d}}};\; F_{\mathrm{k}} = \frac{l_{\mathrm{w}}\rho_{\mathrm{w}}}{4k'_{\mathrm{a}}T}\left(\frac{l_{\mathrm{w}}M_{\mathrm{w}}}{RT} - 1\right),\; F_{\mathrm{d}} = \frac{\rho_{\mathrm{w}}RT}{4e_S^0 D'_{\mathrm{w}}M_{\mathrm{w}}}, \tag{S5}$$

where l_{w} is the latent heat of evaporation of water. Parameters D'_{w} and k'_{a} represent the modified diffusivity (D_{w}) and thermal conductivity (k_{a}), respectively, accounting for non-continuum effects as (Pruppacher and Klett, 2010)

$$k'_{\mathrm{a}} = k_{\mathrm{a}}\Big/\left[1 + \frac{k_a}{\alpha_{\mathrm{T}} r \rho_{\mathrm{w}} c_p}\sqrt{\frac{2\pi M_{\mathrm{a}}}{RT}}\right];\; k_{\mathrm{a}} = 10^{-3}(4.39 + 0.071T), \tag{S6}$$

$$D'_{\mathrm{w}} = D_{\mathrm{w}}\Big/\left[1 + \frac{D_{\mathrm{w}}}{\alpha_{\mathrm{C}} r}\sqrt{\frac{2\pi M_{\mathrm{a}}}{RT}}\right];\; D_{\mathrm{w}} = 2.11 \times 10^{-5}\left(\frac{T}{273.15}\right)^{1.94}\left(\frac{P_0}{P_{\mathrm{T}}}\right), \tag{S7}$$

where we have introduced the heat capacity c_{p} and the thermal accommodation and condensation coefficients, α_{C} and α_{T} respectively (P_0 = 101325 Pa). And, for the purposes of this work, we assume fixed coefficients $\alpha_{\mathrm{T}} = \alpha_{\mathrm{C}} = 1$. If the effects of diffusivity are much greater than thermal conductivity (i.e., $F_{\mathrm{d}} >> F_{\mathrm{k}}$), we can simplify Eq. (S4) and rearrange it into the equivalent form

$$\frac{dr}{dt} = \frac{A}{b_2 r_{\mathrm{w}} + 1};\; \mathrm{A} = \frac{\upsilon\bar{\nu}n_{\mathrm{w}}^{sat}\alpha_{\mathrm{w}}}{4}(S_{\mathrm{e}} - S_{\mathrm{v}}), b_2 = \frac{\bar{\nu}}{4D_{\mathrm{w}}}, \tag{S8}$$

where $\bar{\nu}$ is the mean molecular thermal speed and υ is the molar volume of water. This definition is employed when solving the L_{w} integral within the K15 approach (Ford, 1998, p.20076; Kärcher et al., 2006; Kärcher and Lohmann, 2003) as the functional dependence on r_{w} makes Eq. (S8) more tractable than Eq. (S4).

S3 Limiting behaviour of κ-Köhler theory

We know that the maximum hygroscopicity parameter is on the order $\kappa \sim 1$. Using this value, Eq. (7) in the main text collapses to

$$S_v = \frac{d_\mathrm{w}^3 - d_\mathrm{d}^3}{d_\mathrm{w}^3} e^{\left(\frac{4\sigma_\mathrm{s} M_\mathrm{w}}{RT\rho_\mathrm{w} d_\mathrm{w}}\right)}. \tag{S9}$$

To identify the critical wet particle diameter, $d_{\mathrm{w,c}}$, we can differentiate Eq. (S9) with respect to d_w and set the result equal to zero.

$$\frac{dS_\mathrm{v}}{dd_\mathrm{w}} = \frac{3e^{\frac{a}{d_\mathrm{w}}}}{d_\mathrm{w}} - \frac{e^{\frac{a}{\mathrm{w}}}(-d_\mathrm{d}^3 + d_\mathrm{w}^3)}{d_\mathrm{w}^5} - \frac{3e^{\frac{a}{\mathrm{w}}}(-d_d^3 + d_\mathrm{w}^3)}{d_\mathrm{w}^4} = 0; \quad a = \frac{4\sigma_s M_\mathrm{w}}{RT\rho_\mathrm{w}}, \tag{S10}$$

$$d_{\mathrm{w,c}} = \frac{2^{1/3} d_\mathrm{d}^3}{\left(d_\mathrm{d}^3 \mathrm{a}^3 + \sqrt{-4d_\mathrm{d}^9 \mathrm{a}^3 + d_\mathrm{d}^6 \mathrm{a}^6}\right)^{\frac{1}{3}}} + \frac{\left(d_\mathrm{d}^3 \mathrm{a}^3 + \sqrt{-4d_\mathrm{d}^9 \mathrm{a}^3 + d_\mathrm{d}^6 \mathrm{a}^6}\right)^{\frac{1}{3}}}{2^{1/3}\mathrm{a}}. \tag{S11}$$

To recover the critical water saturation ratio, we can introduce the result from Eq. (S11) into Eq. (S9), which gives us an analytic expression for $S_{\mathrm{v,c}} = S_{\mathrm{v,c}}(a, d_\mathrm{d}, \kappa = 1)$. We find that this analytical function is monotonic, and the solution asymptotically approaches $S_{\mathrm{v,c}} \to 1$ in the limit $d_\mathrm{p} \to \infty$, in agreement with numerical solution used in this work. Therefore, we have demonstrated that within the κ-Köhler framework, even highly hygroscopic materials ($\kappa \sim 1$) cannot achieve critical water saturation ratios that are equivalent to or fall below unity. Only surfaces with zero curvature (plane surfaces) are capable of condensing water at ambient water saturation ratios of unity; for particles with finite diameters, the equality $S_{\mathrm{v,c}} > 1$, is always satisfied.

S4 Extension to lognormal distributions

In the analysis in Sect. 2 of the main text, we have presented arguments under the assumption that all particles within a contrail mixing plume are identical and therefore share the common properties (d_d, κ), which define their activation behaviour. Although this approach is sufficient to gain an insight into the relevance of particle properties, most of the results presented hereafter in this work rely on – and can only be interpreted by - a more sophisticated description of particle properties. To that end, we define a particle type according to its particle size distribution (PSD) (Seinfeld and Pandis, 2016)

$$\frac{dN}{d\ln d_\mathrm{d}} = \frac{N_\mathrm{t}}{\sqrt{2\pi}\ln\sigma_\mathrm{g}} e^{\left[-\frac{(\ln d_\mathrm{d} - \ln d_\mathrm{g})^2}{2(\ln\sigma_\mathrm{g})^2}\right]}, \tag{S12}$$

where N_t represents the total number of particles, σ_g represents the geometric standard deviation (GSD) of the distribution and d_g represents the geometric mean diameter (GMD). Incidentally, the description used in Sect. 2 of the main text is equivalent to taking Eq. (S12) in the limit $\sigma_\mathrm{g} \to 1$, which represents an infinitely narrow distribution comprising particles with a uniform diameter $d_d = d_\mathrm{g}$. Assuming that a given particle type comprises particles with uniform composition and mixing state, we assert that a particle type may be fully described if the properties of its PSD $(d_\mathrm{g}, \sigma_\mathrm{g}, N_\mathrm{t})$ and its total hygroscopicity parameter are known. A consequence of departing from the simplistic description of an infinitely narrow PSD, is that for a given ambient saturation ratio, it is no longer the case that either all or none of the particles are activated (Boolean-type), but rather that some proportion of the particles will be activated. From Sect. 2 of the main text, we know that the critical saturation ratio for activation may be determined if the particle diameter, total hygroscopicity parameter and ambient temperature are known, $S_\mathrm{v,c} = S_\mathrm{v,c}(T, d_\mathrm{d}, \kappa)$. Similarly, this relationship may be inverted to estimate the critical particle diameter, $d_\mathrm{d,c}$, required for activation for a given ambient saturation ratio, $d_\mathrm{d,c} = d_\mathrm{d,c}(T, S_\mathrm{v}, \kappa)$. Because the relationship is monotonic, we know that for a given ambient saturation ratio S_v, all particles with $d_\mathrm{d} > d_\mathrm{d,c}$ will be able to activate. Therefore, for a particle type defined by a total hygroscopicity parameter κ and PSD properties $(d_\mathrm{g}, \sigma_\mathrm{g}, N_\mathrm{t})$, the number of particles that can activate at a given ambient water saturation ratio, S_v, is given by the truncated integral of Eq. (S12) as

$$N = \int_{d_\mathrm{d,c}(T,S_\mathrm{v},\kappa)}^{\infty} \frac{N_\mathrm{t}}{\sqrt{2\pi}\ln\sigma_\mathrm{g}} e^{\left[-\frac{(\ln d_\mathrm{d} - \ln d_\mathrm{g})^2}{2(\ln\sigma_\mathrm{g})^2}\right]} d\ln d_\mathrm{d}. \tag{S13}$$

After changing variables and performing the integration, we arrive at a modified form of the lognormal cumulative distribution function which uses the error function (erf)

$$N = \frac{N_\mathrm{t}}{2}\left[1 - \mathrm{erf}\left(\frac{(\ln d_\mathrm{d,c}(T,S_\mathrm{v},\kappa) - \ln d_\mathrm{g})^2}{2(\ln\sigma_\mathrm{g})^2}\right)\right]. \tag{S14}$$

S5 K15 model extension: particle modes

To extend the description of the ambient particle mode used in K15, results from the global aerosol-climate model ECHAM-HAM (Zhang et al., 2012) were obtained. This model categorises particles into seven classes according to their size and solubility (Vignati et al., 2004): insoluble coarse mode particles and insoluble/soluble nucleation, accumulation and Aitken mode particles. Each class is described by a GMD and GSD and, as an approximation, soluble and insoluble modes are prescribed conservative hygroscopicity parameters of 0.5 and 0 respectively. For the purposes of this work, ECHAM-HAM data for year 2018 were interpolated at the mean altitude of waypoints that satisfied the SAC (Spire Aviation, 2024).

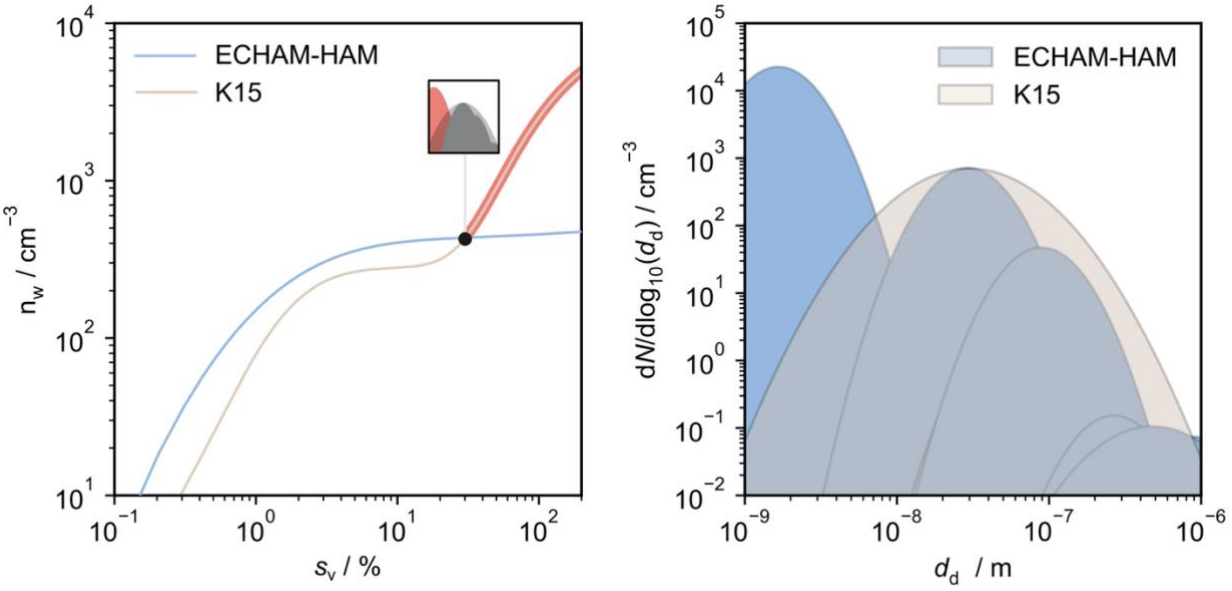

Figure S2: (a) anticipated activated particle number concentration for the original and updated ambient particle modes. Activation of the small, soluble nucleation mode is highlighted, resulting in a pronounced increase in the number concentration of activated particles in the plume (b) comparison of the original and updated ambient particle modes used within the K15 and extended K15 models respectively.

In Fig. S2b, we compare the ambient particle size distribution obtained from the 7-mode ECHAM-HAM model (blue) with the single ambient mode used in the K15 model (beige). The resulting differences in particle activation are shown in Fig. S2a where the total number of activated particles is shown as a function of ambient supersaturation. We find that for moderate supersaturations (s_v < 10 %) both descriptions lead to similar numbers of activated particles. However, if the supersaturation is able to exceed ~ 30 %, the populous soluble nucleation mode is able to activate resulting in a sharp increase in the number of activated particles. Under soot-poor conditions, the absence of a significant condensational sink will typically lead to greater plume supersaturations. Hence, a complete description of the ambient particle mode (including soluble nucleation mode particles) is critical to understanding contrail formation under these conditions (Bier et al., 2022).

S6 K15 model extension: activated fractions

In the K15 model, integration over the PDF to determine activated number concentrations is approximated. The form of the approximation used is given by

$$N \approx \frac{N_t}{1+\left(\frac{d_{\mathrm{d,c}}(T,S_{\mathrm{v}},\kappa)}{d_{\mathrm{g}}}\right)^{\zeta}}, \tag{S15}$$

$$\zeta = \frac{4}{\sqrt{2\pi}} \ln \sigma_{\mathrm{g}}, \tag{S16}$$

where ζ is defined as a size distribution slope parameter.

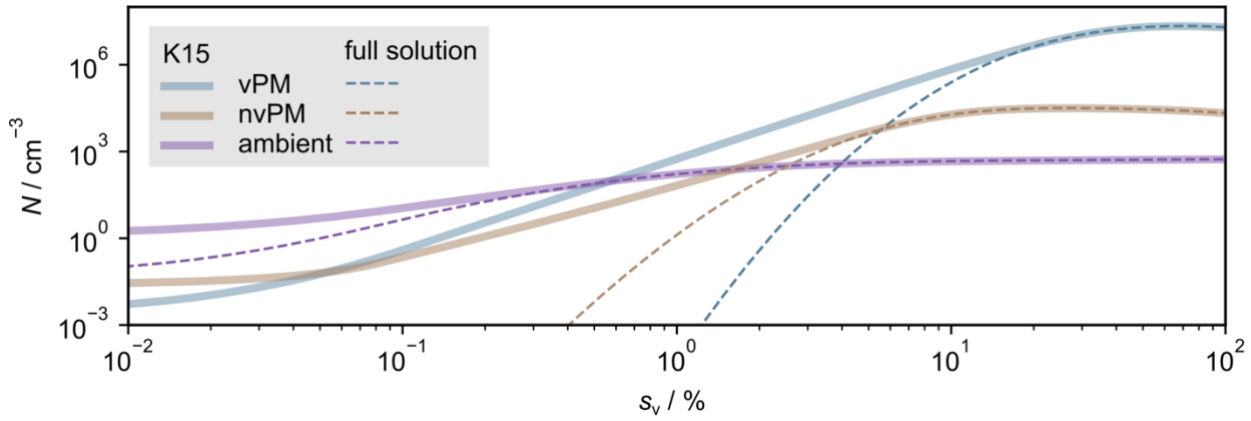

Figure S3: Comparison of the K15 approximation of PDF integration versus full (analytical) solution for the three particle modes as outlined in Table. 1 of the main text.

Fig. S3 shows the agreement between Eq. (S15) and Eq. (S16). Using the particle types outlined in Table. 1 of the main text, we find that for nvPM and ambient particle modes, the K15 approximation is valid for estimates above a supersaturation of ~ 10%. Below this value, the K15 approximation systematically overpredicts activated number concentrations. For the transition and soot-poor regimes, discrepancy between the K15 approximation and the full solution is more prominent, and agreement is only achieved for supersaturations exceeding ~ 20%. For this reason, we choose to use the full solution in our extended K15 model simulations.

S7 K15 model extension: numerical treatment of κ-Köhler theory

In the K15 model, the authors estimate $S_{\mathrm{v,c}}(T, d_{\mathrm{d}}, \kappa)$ using an approximate analytical solution derived from Eq. (7) in the main text, which takes the form

$$\ln S_{\mathrm{v,c}} = \sqrt{\frac{4}{27\kappa}\left(\frac{A}{d_{\mathrm{d}}}\right)^3}\ ;\ A = \frac{4\sigma_{\mathrm{s}} M_{\mathrm{w}}}{RT\rho_{\mathrm{w}}}, \tag{S17}$$

Although analytically tractable, Eq. (S17) is only strictly valid for estimating critical water saturation ratios provided $\kappa >$ 0.2 (Petters and Kreidenweis, 2007). Outside this range, $S_{\mathrm{v,c}}(T, d_{\mathrm{d}}, \kappa)$ must instead be determined by numerical methods.

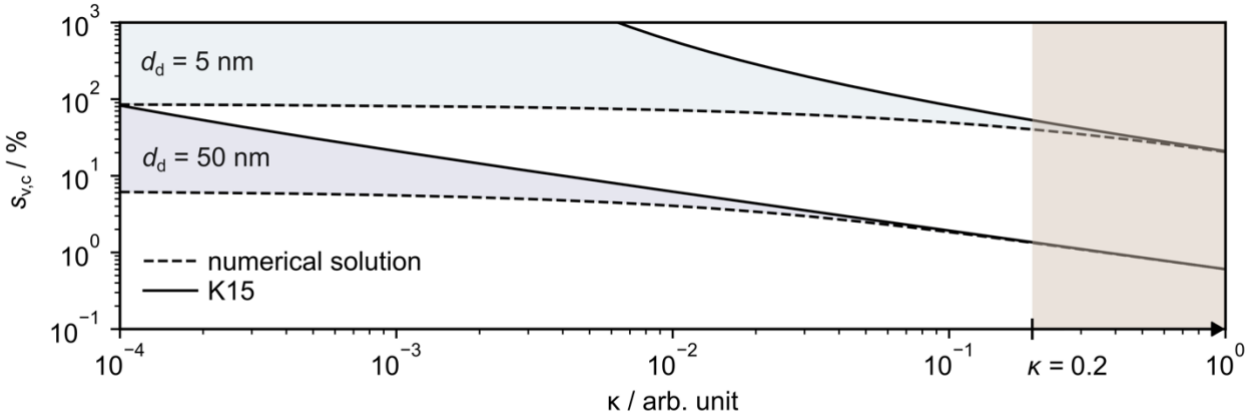

Figure S4: Comparison of numerical versus analytical treatment of *κ*-Köhler theory at *T* = 230 K.

In Fig. S4, we compare the analytical and numerical approaches to estimating $S_{\mathrm{v,c}}$. Estimates have been shown for two dry particle diameters, d_{d} = 5 nm and 50 nm, to highlight the size dependence. In summary, we find that the condition $\kappa > 0.2$ is valid (i.e., the numerical and analytical approximation agree to within ~ 1%) provided $d_{\mathrm{d}} \gtrsim 10$ nm. The approximation collapses for smaller dry particle diameters and overpredicts the numerical result by a factor ~1.3 and ~10 for $d_{\mathrm{d}} = 5$ nm and $d_{\mathrm{d}} = 1$ nm (not shown) respectively (at κ = 0.2). Therefore, for the purposes of this work, the analytical model is strictly applicable for particles that satisfy both $d_{\mathrm{d}} > 10$ nm *and* $\kappa > 0.2$. Whilst these conditions are met for the majority of the nvPM and ambient particles considered in K15, they are not met for smaller vPM particles. Therefore, we choose to apply the full numerical solution to evaluate $S_{\mathrm{v,c}}$ in our extended K15 model simulations, at the cost of a marginal decrease in computational efficiency.

S8 K15 model extension: microphysical term

To determine $n_{\mathrm{w}}^{(2)}(t)$, first we need to identify the temporal dependence of L_{w}. This is achieved by approximating the functional dependence of $\dot{n}_{\mathrm{w}}(t_0)$ as (Ford, 1998)

$$\dot{n}_{\mathrm{w}}(t_0) = \dot{n}_{\mathrm{w}}(t) e^{-\frac{t-t_0}{\tau_{\mathrm{act}}}}, \tag{S18}$$

where τ_{act} is the characteristic timescale of activation within the mixing plume. This prescribes that the largest contribution to $L_{\mathrm{w}}(t)$ occurs from droplet activation and growth within a narrow activation window $(t - t_0) \sim \tau_{\mathrm{act}}$, in a burst-like activation event. For additional justification on the form of the ansatz, the reader is directed to the original texts (Ford, 1998; Kärcher and Lohmann, 2003). Note that Eq. (S18) allows us to define the total number of activated particles in terms of the nucleation rate, $n_{\mathrm{w}}(t) = \dot{n}_{\mathrm{w}}(t)\tau_{\mathrm{act}}$. Hence, using this relation along with Eq. (S18), we can transform Eq. (25) (in the main text) as

$$L_{\mathrm{w}} = \frac{4\pi}{n_{\mathrm{w}}^{\mathrm{sat}} \upsilon} \frac{n_{\mathrm{w}}(t)}{\tau_{\mathrm{act}}} \int_0^{\infty} \mathrm{d}r_0 \frac{dn_{\mathrm{w}}}{dr_0} \int_{-\infty}^{t} e^{-\frac{t-t_0}{\tau_{\mathrm{act}}}} \mathrm{r}_{\mathrm{w}}^2(t, t_0) \dot{r}_{\mathrm{w}}(t, t_0)\, \mathrm{d}t_0, \tag{S19}$$

where we have used the ideal gas law to redefine the prefactor in terms of $n_{\mathrm{w}}^{\mathrm{sat}}$ and υ, the water vapor number density at water saturation and volume of a water molecule in supercooled water, respectively. The definition of the radial growth law, $\dot{r}_{\mathrm{w}}$, is described in more detail in SI S2. Critically, our definition of the radial growth law departs from the definition used in K15 and earlier work (Ford, 1998; Kärcher and Lohmann, 2003), as we have chosen to explicitly incorporate the Kelvin effect. This enables us to more accurately describe water uptake by the smaller vPM mode. For efficient computational models, it is preferable that the solutions to Eq. (S19) are analytic, which is only possible if both integrations can be solved analytically. Therefore, we will next outline several approaches to solving the integrations.

The outer integration takes place over the activated particle size distribution. Although this can be solved numerically, there are also several approximations that can be used to yield compact analytical solutions. In the K15 model, the authors replace this integral using the critical droplet radius, weighted by the available number concentration of each particle type, $\bar{r}_{\mathrm{w,c}}$. This approach assumes that all contributions made at time t_0 are from particles with the critical radius $r_{\mathrm{w,c}}$. However, as we have shown in Sect. 2.2 of the main text, particles with radii $r > r_{\mathrm{w,c}}$ are also able to activate. In other words, it is possible that this approach underestimates the mean activated particle radius at a given time t_0. We explore a replacement for the first integral by using the arithmetic mean particle radius over the truncated activated size distribution, which is then weighted by the available number concentration of each particle type. We denote this as $\tilde{r}_{\mathrm{w,c}}$. We will later show under which circumstances this approach provides better agreement with the numerical solution than the original K15 model approach.

Within the K15 model, the authors perform the inner integration by separating the integral into two cases (Kärcher and Lohmann, 2003). To explain the physical meaning of these cases, we first define the relaxation parameter, κ_{w}, as the ratio of the droplet activation and growth timescales, τ_{act} and τ_{gw} respectively,

$$\kappa_{\mathrm{w}} = \frac{\tau_{\mathrm{act}}}{\tau_{\mathrm{gw}}};\ \tau_{\mathrm{gw}} = \frac{1}{\left(\frac{\partial \ln r_{\mathrm{w}}}{\partial t}\right)} = \frac{r_{\mathrm{w}}(1 + b_2 r_{\mathrm{w}})}{A}, \tag{S20}$$

where the prefactor, A can either include or omit the Kelvin effect and is described in SI S2. This enables us to define the first case as the slow-growth regime, where particle activation dominates over droplet growth and $\kappa_{\mathrm{w}} < 1$. The second case is the fast-growth regime, where droplet growth dominates over particle activation and $\kappa_{\mathrm{w}} > 1$. These cases permit us to prescribe limiting behaviour in the droplet growth law, thereby eliminating the t-dependence in Eq. (S19). For a full description of this method, the reader is directed to Kärcher and Lohmann, 2003. When the Kelvin effect is not included in the growth law, analytical solutions for the inner integration can be determined in both the slow- and fast-growth regimes. On the other hand, incorporating the Kelvin effect within the radial growth law precludes an analytical approach, and the resulting expression can only be solved numerically. However, the slow-growth regime can still be solved analytically, and the solution is given by

$$L_w = \frac{4\pi \bar{r}_{\mathrm{w,c}}^3 n_{\mathrm{w}}(t)}{n_{\mathrm{w}}^{\mathrm{sat}} \tau_{\mathrm{gw}} \upsilon} (2\kappa_{\mathrm{w}}^2 + 2\kappa_{\mathrm{w}} + 1), \tag{S21}$$

including our earlier approximating regarding the outer integration. If the Kelvin effect is omitted, it is also possible to solve Eq. (S19) analytically for all growth regimes as described in Kärcher et al. (2006).

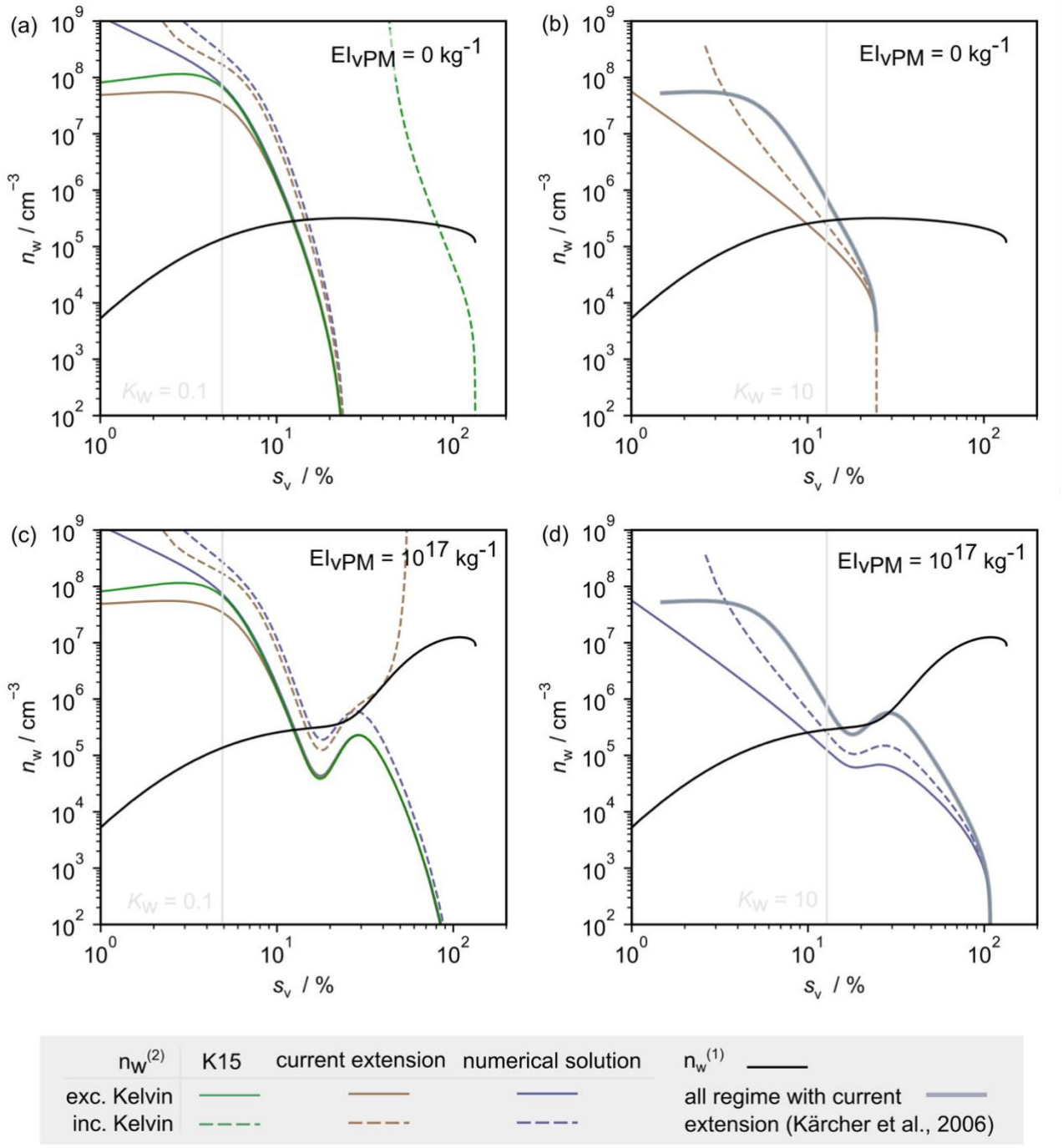

Figure S5: variation of $n_w^{(2)}$ and $n_w^{(1)}$ with increasing plume supersaturation for T_A = 215 K and G = 1.64 PaK^{-1} in the soot-rich regime (EI$_{nvPM}$ = 10^{15} kg^{-1}), using the particle properties for GMD, GSD and κ defined in Table of the main text. In panels (a) and (b), EI$_{vPM}$ = 0 kg^{-1} (as in the original K15 model) whereas in panels (c) and (d), EI$_{vPM}$ = 10^{17} kg^{-1}. In panels (a) and (c) $n_w^{(2)}$ has been computed for the *slow*-growth regime with inclusion (inc.) and exclusion (exc.) of the Kelvin effect. For each of these, the outer integral has been estimated using three approaches: solving numerically (thinner purple lines), using the B15 model (green lines) and using our extension (brown lines). In panels (b) and (d) $n_w^{(2)}$ has been computed for the *fast*-growth regime with inclusion (inc.) and exclusion (exc.) of the Kelvin effect. Also, results valid across all regimes have been plotted (thicker purple lines), excluding the Kelvin effect (Kärcher et al., 2006). In each case, the outer integral has been estimated using our extension. In panel (a/c) and (b/d), vertical lines have also been shown corresponding to $\kappa_w = 0.1$ and $\kappa_w = 10$ respectively, defining the approximate limits of applicability according to Eq. (S20).

In Fig. S5, we have demonstrated how $n_{\mathrm{w}}^{(1)}$ and $n_{\mathrm{w}}^{(2)}$ vary with plume supersaturation under typical contrail-forming conditions (T_{A} = 215 K, G = 1.64 PaK^{-1}). These have been estimated in the soot-rich regime (EI$_{\mathrm{nvPM}}$ = 10^{15} kg^{-1}) with and without vPM, using particle characteristics outlined in Table. 1 of the main text. In Fig. S5a, we show the variation of $n_{\mathrm{w}}^{(2)}$ deriving from the solutions for L_{w} in the slow-growth regime. We find that within its range of validity ($\kappa_{\mathrm{w}} < 0.1$), incorporating the Kelvin effect can have a pronounced impact on estimates for soot-rich conditions. In all cases, inclusion of the Kelvin effect acts to increase the effective number of contrail ice crystals, n_{i}. This is because inclusion of the Kelvin effect suppresses the radial growth of water droplets, see Eq. (S8). Moreover, the size-dependence of the Kelvin effect means that if the available particles are smaller, the effect will be more pronounced. This is illustrated in Fig. S5c, where the relative difference between the solid (exc. Kelvin effect) and dashed (inc. Kelvin effect) lines increases dramatically once vPM activation becomes dominant (for $s_{\mathrm{v}} > 30\%$) and $\tilde{r}_{\mathrm{w,c}}$ approaches $d_{\mathrm{g,vPM}}$. We can also use Fig. S5a to compare the various approaches to evaluating the outer integral. Taking the numerical approach as a benchmark, we find better agreement using our approach than the original K15 approach, provided the Kelvin effect is *included*. This is due to the exponential dependence in Eq. (7) of the main text, which is highly sensitive to the choice of mean activated particle radius ($\bar{r}_{\mathrm{w,c}}$ or $\tilde{r}_{\mathrm{w,c}}$). However, when the Kelvin effect is omitted, both approaches provide comparable results and here we choose to use the original K15 approach. Additionally, we find that when the vPM mode is included, it is no longer feasible to estimate $n_{\mathrm{w}}^{(2)}$ for the slow growth regime using the K15 approach with incorporation of the Kelvin effect. For this reason, there is no dashed green line shown in Fig. S5c.

In Fig. S5b and Fig. S5d, we show fast-growth regime solutions that include our outer integral extension with and without inclusion of the Kelvin effect. Inclusion of the Kelvin effect is relatively less impactful in the fast-growth regime solutions compared to the corresponding slow-growth solutions. This aligns with intuition, as when the microphysical term is dominated by droplet growth (as opposed to activation), the initial aerosol properties become less important (Kärcher et al., 2006). In Fig. S5b and Fig. S5d we also show the solution originally derived in Kärcher et al. (2006) that is valid across both regimes (albeit without inclusion of the Kelvin effect) and illustrate its consistency with the slow- and fast-growth solutions under their respective ranges of validity. Critically, when vPM particles are incorporated in the model – see Fig. S5c and Fig. S5d – the intersection of $n_{\mathrm{w}}^{(1)}$ and $n_{\mathrm{w}}^{(2)}$ occurs for $\kappa_{\mathrm{w}} > 10$ and therefore should only be described using solutions for the fast-growth regime. For this reason, we have chosen to adopt the result outlined by Kärcher et al. (2006), which is applicable across all growth regimes. In doing so, we are forced to omit the Kelvin effect and our updated approach for estimating

S9 Model sensitivity to number of vPM modes

In our model, we assume that all vPM particles have identical chemical composition, which is encompassed by the prescribed total hygroscopicity parameter, κ. Due to the nature of vapour condensation in the nascent plume, it is possible that the vPM mode may be distributed into several particle types with different chemical composition (Cantin et al., 2024; Yu et al., 1999). To explore the impact of the aforementioned model assumption, we have divided the vPM mode into two distinct modes: vPM-1 and vPM-2, see Table. S1. This is consistent with experimental measurements of chemi-ions, which show that positive chemi-ions (vPM-2) are mostly comprised of protonated organic material (Kiendler et al., 2000b; Sorokin and Arnold, 2006) while negative chemi-ions (vPM-1) are mostly comprised of deprotonated acidic moieties (derivatives of nitric and sulphuric acid) (Kiendler et al., 2000a). As in our original approach, we can effectively modify the chemical composition of vPM-2 by altering the value of κ associated with it. Finally, we have assumed that the concentrations of vPM-1 and vPM-2 are equivalent ($EI_{vPM\text{-}1} = EI_{vPM\text{-}2}$), in line with in-situ observations (Haverkamp et al., 2004).

Table. S1: particle properties for simulations comprising two vPM modes: vPM-1 and vPM-2.

Mode properties	EI / kg^{-1}	d_g / nm	$\boldsymbol{\sigma_g}$ / no units	κ / no units
Plume vPM-1	5×10^{16}	2.5	1.3	0.5 (H_2SO_4)
Plume vPM-2	5×10^{16}	2.5	1.3	0 – 0.5 (organic material)
nvPM	$10^{12} – 10^{15}$	35	2.0	0.005
ambient	600 cm^{-3}	30	2.2	0.5

As anticipated, we find that when the composition of vPM-2 is purely sulphuric acid, results are equivalent to assuming a single vPM mode as shown in Fig. 7 of the main text (see Fig. S6). When dividing the vPM mode into a mode comprising sulphuric acid and another comprising organic material, AEI_{ice} estimates depend on the chemical composition of vPM-2. As the hygroscopicity of the vPM-2 mode is reduced, a reduced proportion of these particles activate to form water droplets (and freeze to form ice crystals). Ultimately, when the hygroscopicity of this mode has been reduced below $\kappa = 0.01$, AEI_{ice} derives exclusively from vPM-1. Therefore, the effective result is a reduction in AEI_{ice}. Notably, the effect of dividing the vPM mode in two distinct modes with different values of κ is similar to assuming a single mode with a lower mean value of κ. Therefore, we assert that our sensitivity analysis in Fig. 9 of the main text is sufficient to cover the physical possibility of a more complicated, multicomponent vPM mode. Additionally (as demonstrated in Fig. S6), our model is sufficiently flexible to incorporate additional vPM complexity when the properties of this mode are experimentally grounded.

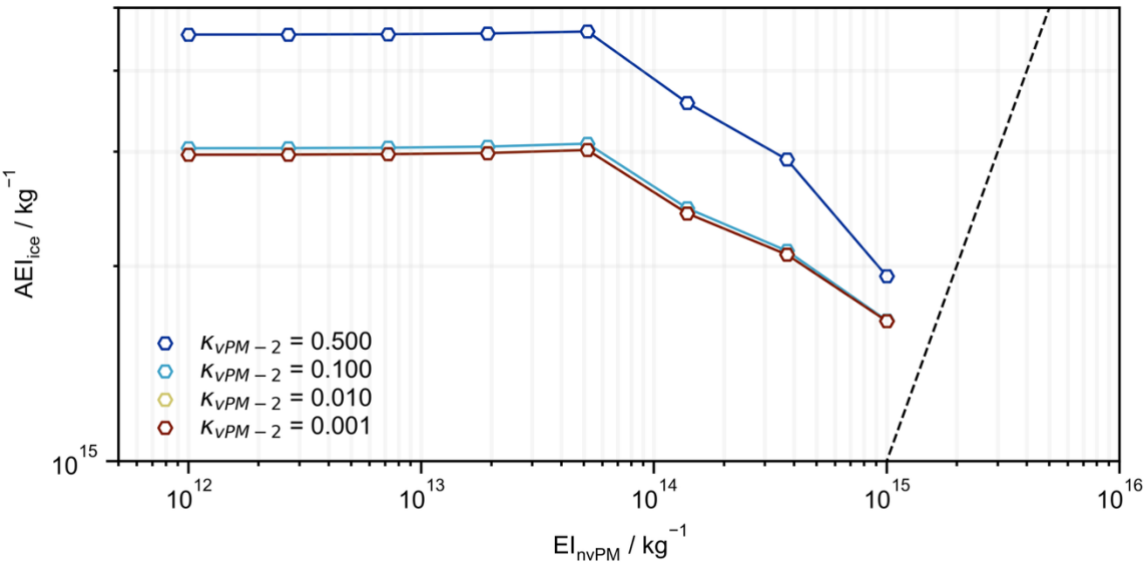

Figure S6: AEI_{ice} sensitivity to EI_{nvPM} and the chemical composition of vPM-2. Note, due to the large increase in the number of tracked size bins when incorporating the additional vPM mode, estimates at large values of EI_{nvPM} (> 10^{15} kg^{-1}) could not be obtained.

S10 Model sensitivity to nvPM particle size

The properties of aircraft nvPM particles can be investigated by performing ground-based measurements behind turbofan engines (Saffaripour et al., 2020). Primary particle size distribution characteristics are typically determined offline, using samples collected for Transmission Electron Microscopy (TEM). Image analysis software is then used to extract information from individual samples, including aggregate scaling properties, the geometric mean primary particle diameter ($d^{(p)}_{g,nvPM}$) and geometric standard deviation ($\sigma^{(p)}_{g,nvPM}$) (Sipkens et al., 2023). Using Table. 2 in Saffaripour et al. (2020), we have selected and/or extracted relevant primary particle size distribution characteristics for samples collected at 100% thrust from turbofan engines burning Jet A-1, which were obtained from TEM images. To that end, using data from (a) Liati et al. (2014): $d^{(p)}_{g,nvPM}$ = 17.4 nm, $\sigma^{(p)}_{g,nvPM}$ = 1.54; (b) Marhaba et al. (2019): $d^{(p)}_{g,nvPM}$ = 13.5 nm, $\sigma^{(p)}_{g,nvPM}$ = 1.50 and (c) Delhaye et al. (2017): $d^{(p)}_{g,nvPM}$ = 16.1 nm, $\sigma^{(p)}_{g,nvPM}$ = 1.50, we estimate average primary particle size distribution characteristics $d^{(p)}_{g,nvPM}$ = 15.7 ± 1.6 nm and $\sigma^{(p)}_{g,nvPM}$ = 1.50 ± 0.02. Given our choice of geometric mean aggregate particle diameter ($d^{(a)}_{g,nvPM}$ = 35 nm), the ratio of mean primary-to-aggregate particle sizes is XR = 0.45, which is similar to the baseline value XR = 0.41 used in Yu et al. (2024). However, here we choose to discriminate between primary or aggregate particle size distribution characteristics using the superscript (p)/(a) as both the GMD *and* the GSD are modified.

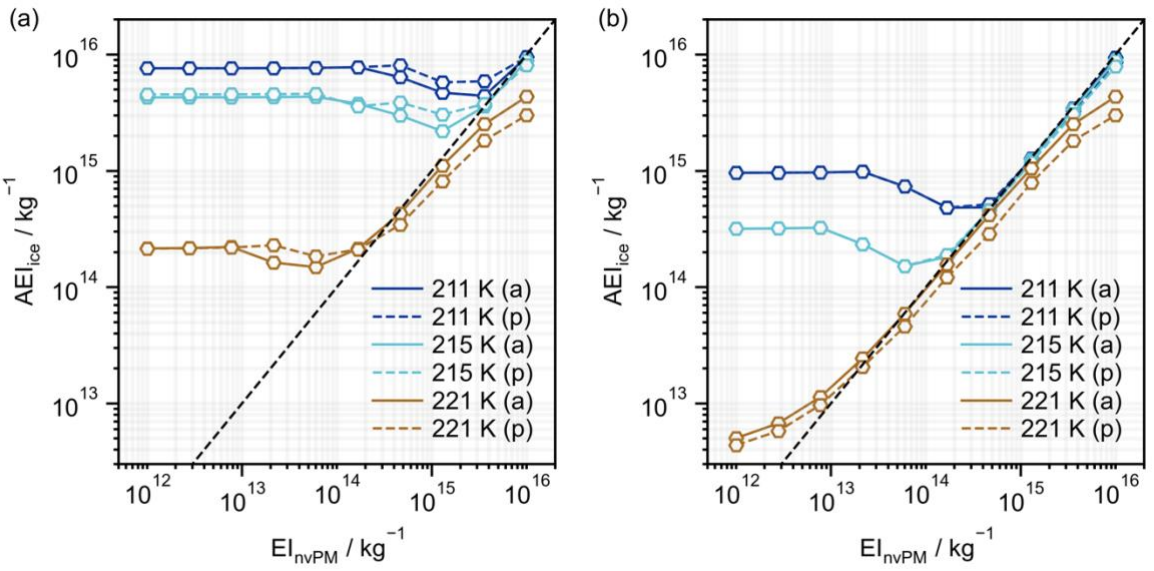

Figure S7: apparent ice emission index at 230 K (hexagonal markers) and its dependence on T_A and EI_{nvPM} for (a) sulphur-rich and (b) organic-rich volatile particles. The impact of assuming aggregate "(a)" or primary "(p)" particle size distribution characteristics, GMD and GSD of (35 nm, 2.0) and (15.7, 1.5) respectively, is shown.

Fig. S7 shows AEI_{ice} sensitivity to T_A, EI_{nvPM} and the choice of either nvPM primary particles or aggregates, using (a) sulphur-rich and (b) organic-rich vPM properties as described in Sect. 3.4 of the main text. For temperatures close to T_{SAC}, AEI_{ice} is reduced if most droplets are formed via nvPM. This is because for a given plume supersaturation, more nvPM aggregate particles are able to activate than nvPM primary particles, due to the larger GMD and GSD. Therefore, when $EI_{nvPM} = 10^{16}$ – which precludes substantial vPM activation in the case of both sulphur- and organic-rich vPM - AEI_{ice} is reduced by 30% when using nvPM primary particles compared to aggregates. For sulphur-rich conditions, as the minimum is approached from high EI_{nvPM} which implies competition between vPM and nvPM, AEI_{ice} is increased by up to 40% when using nvPM primary particles compared to aggregates. Again, this occurs because fewer nvPM primary particles are able to activate at a given supersaturation compared to aggregates, so the more numerous vPM mode is able to compete for available water vapour at a higher EI_{nvPM}.

Overall, we find that upon changing our description from nvPM aggregates to primary particles: (i) if most water droplets form via nvPM, AEI_{ice} is reduced as a smaller proportion of the nvPM size distribution can activate and (ii) if a large proportion of droplets form via vPM (i.e., the minimum in Fig. S7), AEI_{ice} is increased as nvPM provides less competition for available supersaturation and (iii) for sulphur-rich vPM, (i) + (ii) lead to an effective translation of the aggregate profiles in Fig. S7 (a) towards increased EI_{nvPM}. Each of these results is qualitatively consistent with the findings in Yu et al. (2024).

S11 Pyrcel uncertainty estimate

In pyrcel, changing the number of size bins for a given mode changes the discretization of particle diameters. Given the parameterization for activation is highly sensitive to particle diameter (see Eq. (9) in the main text), small adjustments to these values can therefore impact activated particle number concentrations and AEI_{ice}. During our analyses, we noticed that AEI_{ice} was more sensitive to the prescribed number of size bins for vPM than for nvPM. We suggest that this is likely a consequence of two factors. Firstly, $d_{g,vPM}$ is smaller than $d_{g,nvPM}$ (see Table. 1 in the main text) and activated number concentrations are increasingly sensitive to smaller particle diameters (see Fig. 2b in the main text). Secondly, the droplet and ice (see Fig. S8) particle size distributions for nvPM and vPM have different forms. For nvPM, the maximum in the ice particle size distribution is distinctly separated from the minimum diameter of activation. However, for vPM, the maximum in the ice particle size distribution *is* equivalent to the minimum diameter of activation. As a result, small changes in the quantization of size bins (that modify the minimum diameter of activation) have a large effect on the number concentration of vPM-derived ice crystals but not on the concentration of nvPM-derived ice crystals.

For this reason, we decided to interrogate model sensitivity to the prescribed number of (n)vPM size bins. We chose to investigate the sensitivity under soot-poor conditions ($EI_{nvPM} = 10^{12}$ kg^{-1}) as this represents the point at which AEI_{ice} is maximally sensitive to vPM. Therefore, we can use the sensitivity at this point to derive maximum uncertainties. Accordingly, simulations were performed using a sulphur-rich plume vPM mode (according to Table. 1 in the main text), $T_A = 215$ K and $EI_{nvPM} = 10^{12}$ kg^{-1}. When varying the number of vPM size bins, other size bin numbers were fixed at 50. Model sensitivity to the number of vPM size bins is shown in Fig. S9.

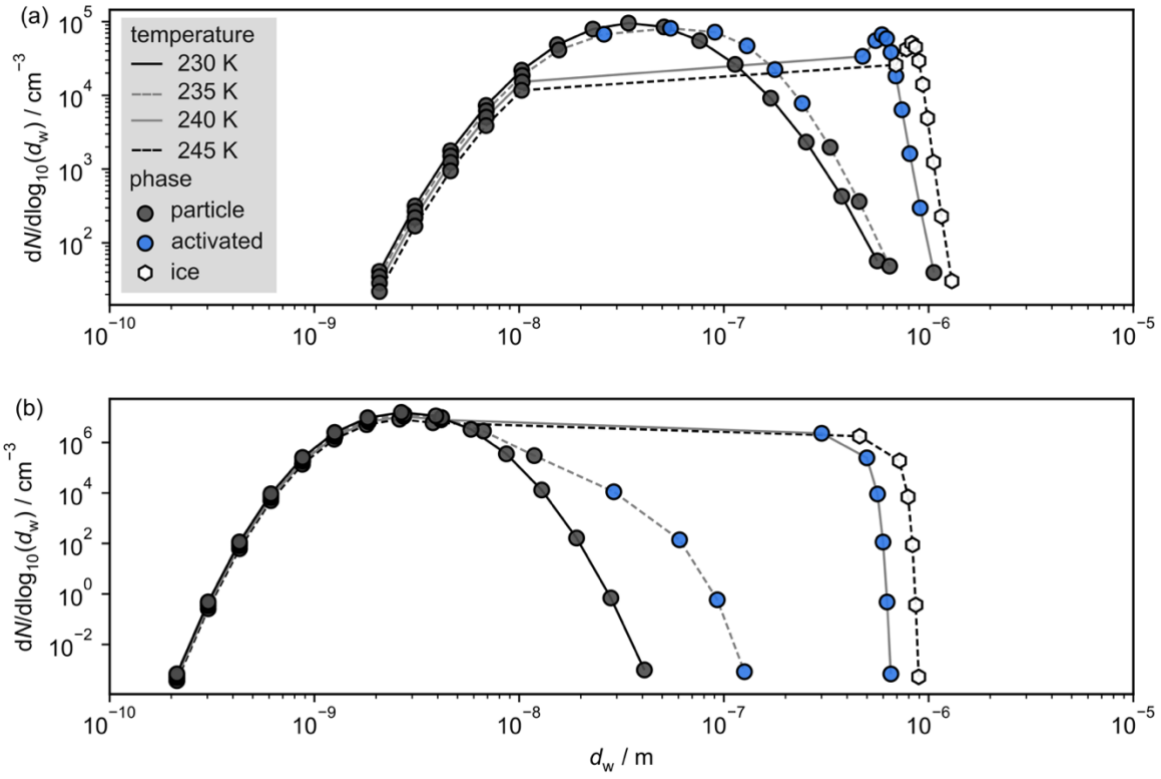

Figure S8: particle size distributions for (a) nvPM and (b) vPM illustrative of typical contrail mixing behaviour. The particle size distributions have been shown at four different temperatures during plume evolution and the phase (solid/liquid aerosol, liquid droplet, ice crystal) of each bin has been indicated using a different marker.

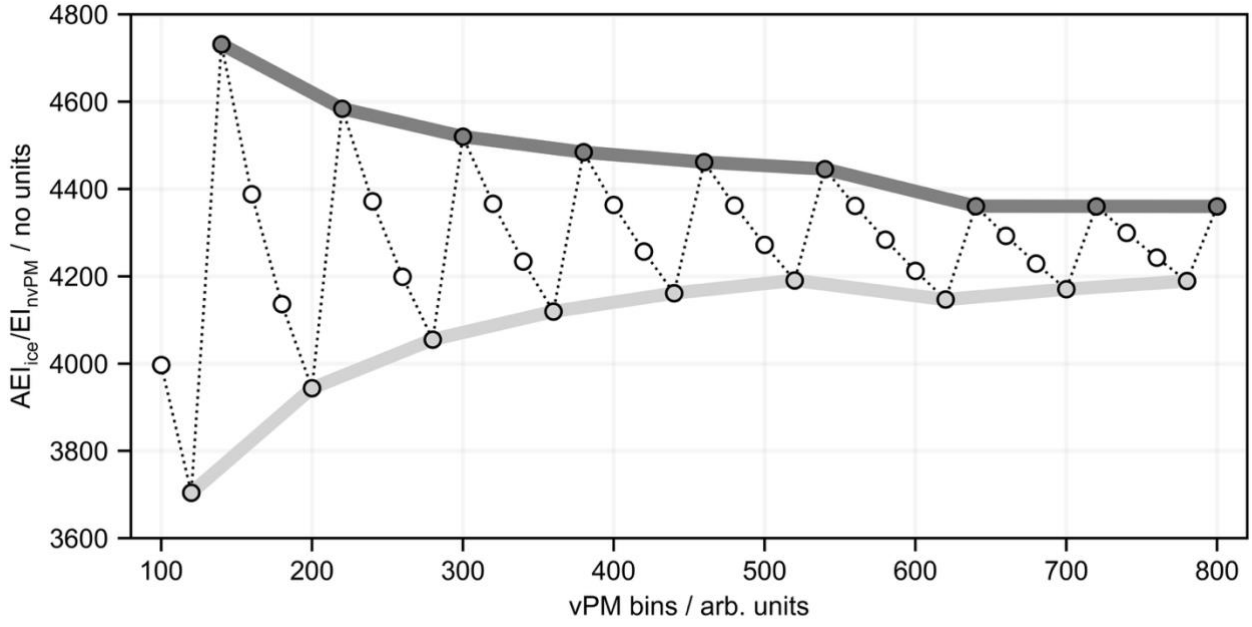

Figure S9: AEI_{ice} sensitivity (normalised by $EI_{nvPM} = 10^{12}$ kg^{-1}) to the number of size bins prescribed for vPM. An envelope is drawn to constrain maximum errors associated with each vPM bin number.

Previously, we found that AEI_{ice} estimates were largely insensitive to the number of prescribed nvPM size bins. However, for vPM, we find that AEI_{ice} estimates converge with increasing numbers of size bins. By enveloping these estimates, we find that errors range from -10% to +9% for 150 size bins, which is the typical number used in our model simulations. Therefore, this represents the maximum uncertainty in our AEI_{ice} estimates.

S12 Upper tropospheric ambient temperatures

Meteorological and Automatic Dependent Surveillance-Broadcast (ADS-B) data were obtained from Spire Aviation (Spire Aviation, 2024) and ECMWF respectively for the date 01/01/2019. The purpose of this analysis is to assess the upper tropospheric lapse rate at typical contrail-forming altitudes and comment on implications for temperature-based contrail avoidance.

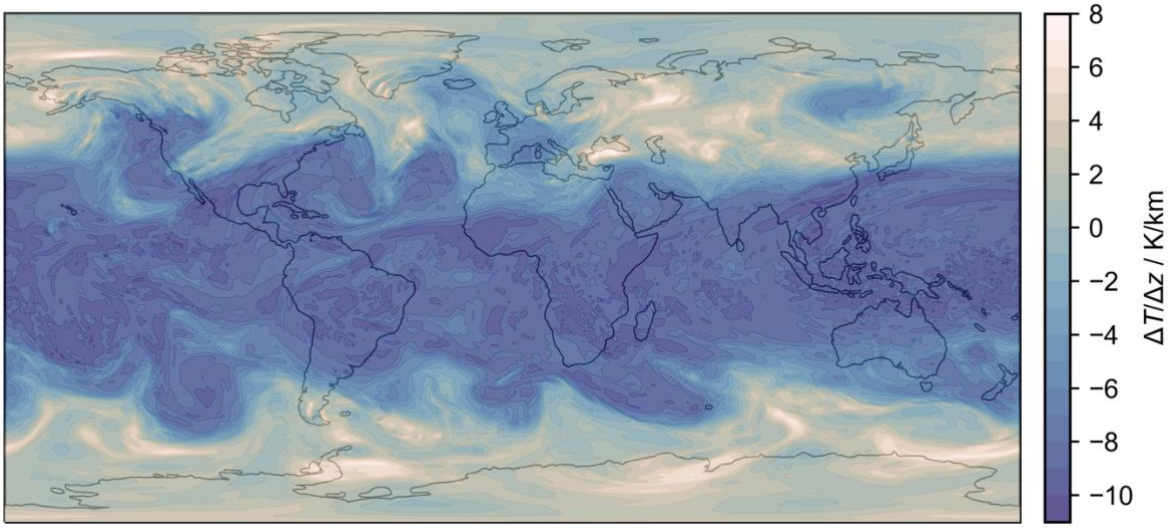

Figure S10: upper tropospheric lapse rate ($\Delta T/\Delta z$) at the mean contrail-forming altitude obtained for flight waypoints satisfying the SAC using the Spire and ECMWF datasets for 01/01/2019.

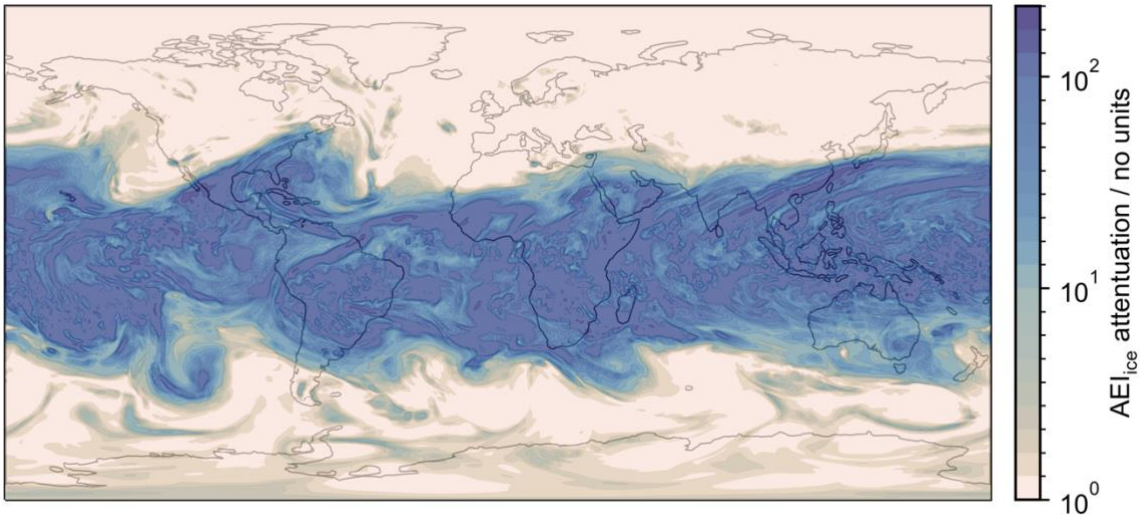

Figure S11: attenuation in AEI_{ice} achieved for soot-poor conditions ($EI_{nvPM} = 10^{12}$ kg^{-1}) with deviations of ± 10 flight levels from the mean contrail-forming altitude.

Fig. S10 shows how the upper tropospheric lapse rate ($\Delta T/\Delta z$) calculated at the mean contrail-forming altitude (contrail waypoints that satisfy the SAC) varies as a function of longitude and latitude. We find that within the tropics (± 23.5°), the lapse rate is approximately – (8 ± 1) K/km; the temperature increases with a decrease in altitude. Here, ambient temperature changes of ~2 K are possible by reducing cruise altitudes by ± 10 flight levels (1000 ft). By contrast, in the extratropical regions, the lapse rate exhibits greater variation and can be positive.

In Fig. 9 of the main text, we presented the dependence of AEI_{ice} on ambient temperature for various emissions scenarios. Using these data with the information in Fig. S10, we can estimate the reduction in AEI_{ice} (without sublimation losses) that could be achieved by altering flight altitudes by ± 10 flight levels. For the purpose of this discussion, we have focussed on the soot-poor regime, where the greatest attenuation of the apparent emission index of ice ($AEI_{ice,\ unadjusted}$ / $AEI_{ice,\ with\ altitude\ adjustment}$) is possible (see Fig. 9 of the main text). We find that attenuations exceeding 100 are achievable in the tropics by reducing flight altitudes by 10 flight levels. Smaller attenuations are achievable in the extratropical regions as the ambient temperature at the mean contrail-forming altitude is cooler.

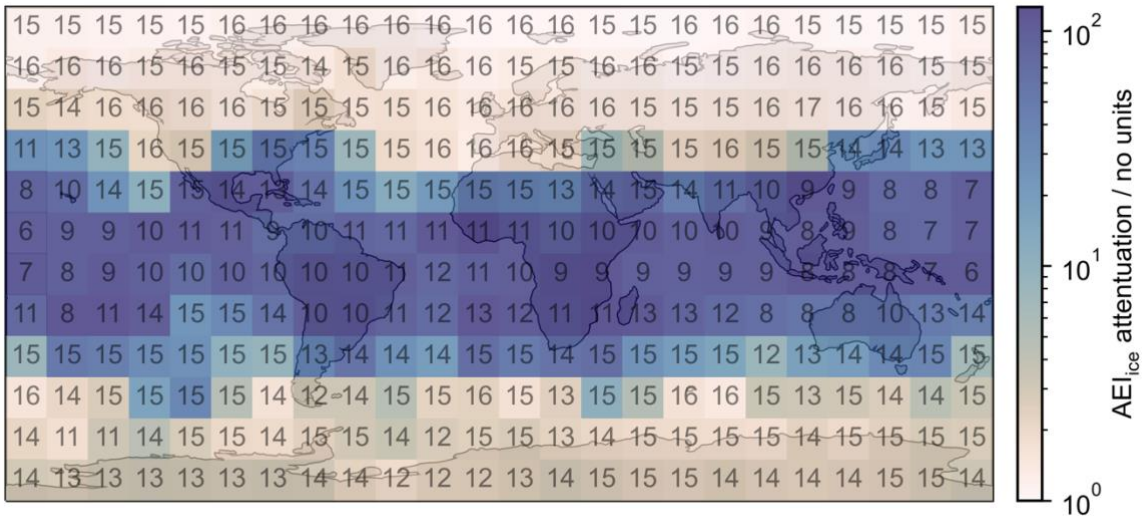

Figure S12: attenuation in AEI_{ice} as in Fig. S11. The value of $\log_{10}(AEI_{ice})$ at the mean contrail-forming altitude has also been marked on each grid cell for reference.

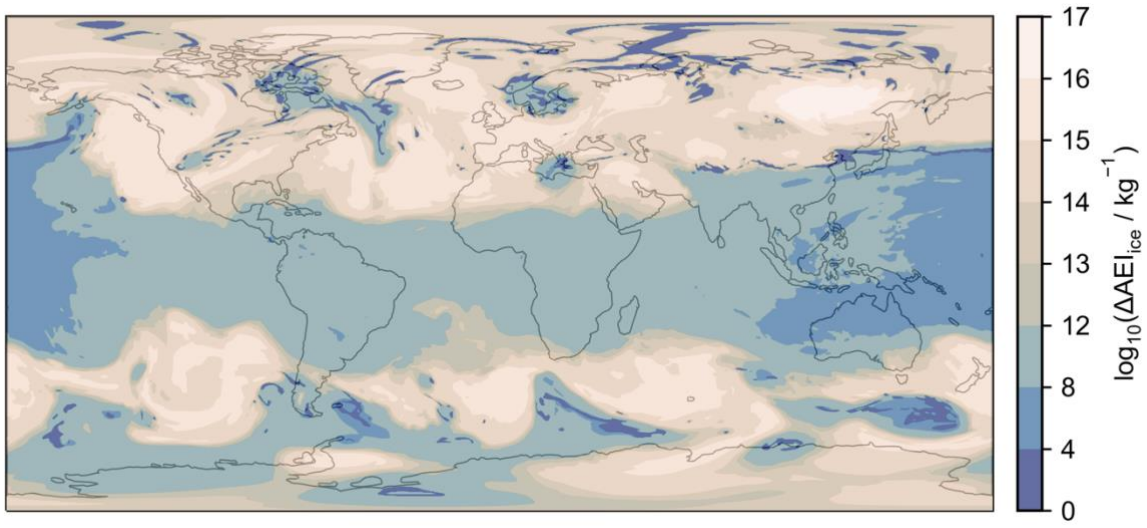

Figure S13: absolute reduction in AEI_{ice} achieved for soot-poor conditions ($EI_{nvPM} = 10^{12}$ kg^{-1}) with deviations of ± 10 flight levels from the mean contrail-forming altitude.

Although larger attenuations are achieved in the tropics compared to the extratropical regions, warmer ambient temperatures mean that absolute AEI_{ice} emissions at the mean contrail-forming altitude are typically lower, see Fig. S13. Absolute reductions in AEI_{ice} ($AEI_{ice,\ unadjusted}$ - $AEI_{ice,\ with\ altitude\ adjustment}$) therefore provide a more suitable metric for targeting the most warming contrails, which are associated with larger AEI_{ice} (Teoh et al., 2022). To that end, we find that the largest absolute reductions in AEI_{ice} are found in the northern midlatitudes (~ 30° - 60°). This covers some of the densest regions of global air traffic, including Europe and North America (Teoh et al., 2023). Moreover, the above analysis was performed using meteorological data during winter in the Northern Hemisphere. During the summer months, upper tropospheric temperatures in the Northern Hemisphere are warmer so the potential for temperature-based mitigation in this region is improved. Overall, avoiding cooler regions of the atmosphere may provide an alternative strategy for contrail mitigation.

References

Spire Aviation: https://spire.com/wiki/how-ads-b-has-shaped-the-modern-aviation-industry/, last access: 19 December 2024.

Baumgartner, M., Rolf, C., Grooß, J.-U., Schneider, J., Schorr, T., Möhler, O., Spichtinger, P., and Krämer, M.: New investigations on homogeneous ice nucleation: the effects of water activity and water saturation formulations, Atmospheric Chemistry and Physics, 22, 65–91, https://doi.org/10.5194/acp-22-65-2022, 2022.

Bier, A., Unterstrasser, S., and Vancassel, X.: Box model trajectory studies of contrail formation using a particle-based cloud microphysics scheme, Atmos. Chem. Phys., 22, 823–845, https://doi.org/10.5194/acp-22-823-2022, 2022.

Cantin, S., Chouak, M., and Garnier, F.: Eulerian–Lagrangian CFD-microphysics modeling of aircraft-emitted aerosol formation at ground-level, Aerosol Science and Technology, 58, 1347–1370, https://doi.org/10.1080/02786826.2024.2395940, 2024.

Delhaye, D., Ouf, F.-X., Ferry, D., Ortega, I. K., Penanhoat, O., Peillon, S., Salm, F., Vancassel, X., Focsa, C., Irimiea, C., Harivel, N., Perez, B., Quinton, E., Yon, J., and Gaffie, D.: The MERMOSE project: Characterization of particulate matter emissions of a commercial aircraft engine, Journal of Aerosol Science, 105, 48–63, https://doi.org/10.1016/j.jaerosci.2016.11.018, 2017.

Ford, I.: Ice nucleation in jet aircraft exhaust plumes, in: Pollution from aircraft emissions in the North Atlantic flight corridor (POLINAT 2): final report, Office for Official Publ. of the European Communities, Luxembourg, 269–287, 1998.

Haverkamp, H., Wilhelm, S., Sorokin, A., and Arnold, F.: Positive and negative ion measurements in jet aircraft engine exhaust: concentrations, sizes and implications for aerosol formation, Atmospheric Environment, 38, 2879–2884, https://doi.org/10.1016/j.atmosenv.2004.02.028, 2004.

Kärcher, B. and Lohmann, U.: A parameterization of cirrus cloud formation: Heterogeneous freezing, Journal of Geophysical Research: Atmospheres, 108, https://doi.org/10.1029/2002JD003220, 2003.

Kärcher, B., Hendricks, J., and Lohmann, U.: Physically based parameterization of cirrus cloud formation for use in global atmospheric models, Journal of Geophysical Research: Atmospheres, 111, https://doi.org/10.1029/2005JD006219, 2006.

Kärcher, B., Burkhardt, U., Bier, A., Bock, L., and Ford, I. J.: The microphysical pathway to contrail formation, JGR Atmospheres, 120, 7893–7927, https://doi.org/10.1002/2015JD023491, 2015.

Kiendler, A., Aberle, S., and Arnold, F.: Negative chemiions formed in jet fuel combustion: new insights from jet engine and laboratory measurements using a quadrupole ion trap mass spectrometer apparatus, Atmospheric Environment, 34, 2623–2632, https://doi.org/10.1016/s1352-2310(99)00475-6, 2000a.

Kiendler, A., Aberle, S., and Arnold, F.: Positive ion chemistry in the exhaust plumes of an air craft jet engine and a burner: investigations with a quadrupole ion trap mass spectrometer, Atmospheric Environment, 34, 4787–4793, https://doi.org/10.1016/s1352-2310(00)00253-3, 2000b.

Koop, T., Luo, B., Tsias, A., and Peter, T.: Water activity as the determinant for homogeneous ice nucleation in aqueous solutions, Nature, 406, 611–614, https://doi.org/10.1038/35020537, 2000.

Lewellen, D. C.: A Large-Eddy Simulation Study of Contrail Ice Number Formation, Journal of the Atmospheric Sciences, 77, 2585–2604, https://doi.org/10.1175/JAS-D-19-0322.1, 2020.

Liati, A., Brem, B. T., Durdina, L., Vögtli, M., Arroyo Rojas Dasilva, Y., Dimopoulos Eggenschwiler, P., and Wang, J.: Electron Microscopic Study of Soot Particulate Matter Emissions from Aircraft Turbine Engines, Environ. Sci. Technol., 48, 10975–10983, https://doi.org/10.1021/es501809b, 2014.

Marcolli, C.: Technical note: Fundamental aspects of ice nucleation via pore condensation and freezing including Laplace pressure and growth into macroscopic ice, Atmos. Chem. Phys., 20, 3209–3230, https://doi.org/10.5194/acp-20-3209-2020, 2020.

Marhaba, I., Ferry, D., Laffon, C., Regier, T. Z., Ouf, F.-X., and Parent, P.: Aircraft and MiniCAST soot at the nanoscale, Combustion and Flame, 204, 278–289, https://doi.org/10.1016/j.combustflame.2019.03.018, 2019.

Murray, B. J., Broadley, S. L., Wilson, T. W., Bull, S. J., Wills, R. H., Christenson, H. K., and Murray, E. J.: Kinetics of the homogeneous freezing of water, Phys. Chem. Chem. Phys., 12, 10380–10387, https://doi.org/10.1039/C003297B, 2010.

Murray, B. J., O'Sullivan, D., Atkinson, J. D., and Webb, M. E.: Ice nucleation by particles immersed in supercooled cloud droplets, Chem. Soc. Rev., 41, 6519, https://doi.org/10.1039/c2cs35200a, 2012.

Petters, M. D. and Kreidenweis, S. M.: A single parameter representation of hygroscopic growth and cloud condensation nucleus activity, Atmospheric Chemistry and Physics, 7, 1961–1971, https://doi.org/10.5194/acp-7-1961-2007, 2007.

Pruppacher, H. R. and Klett, J. D.: Microphysics of clouds and precipitation, 2nd ed., Springer Dordrecht, Dordrecht, 2010.

Rogers, R. R. and Yau, M. K.: A short course in cloud physics, Third edition., Butterworth-Heinemann, Burlington, Massachusetts, 1 pp., 1996.

Saffaripour, M., Thomson, K. A., Smallwood, G. J., and Lobo, P.: A review on the morphological properties of non-volatile particulate matter emissions from aircraft turbine engines, Journal of Aerosol Science, 139, 105467, https://doi.org/10.1016/j.jaerosci.2019.105467, 2020.

Seinfeld, J. H. and Pandis, S. N.: Atmospheric chemistry and physics: from air pollution to climate change, 3rd ed., John Wiley & Sons, Inc, Hoboken, New Jersey, 2016.

Sipkens, T. A., Boies, A., Corbin, J. C., Chakrabarty, R. K., Olfert, J., and Rogak, S. N.: Overview of methods to characterize the mass, size, and morphology of soot, Journal of Aerosol Science, 173, 106211, https://doi.org/10.1016/j.jaerosci.2023.106211, 2023.

Sorokin, A. and Arnold, F.: Organic positive ions in aircraft gas-turbine engine exhaust, Atmospheric Environment, 40, 6077–6087, https://doi.org/10.1016/j.atmosenv.2006.05.038, 2006.

Teoh, R., Schumann, U., Gryspeerdt, E., Shapiro, M., Molloy, J., Koudis, G., Voigt, C., and Stettler, M. E. J.: Aviation contrail climate effects in the North Atlantic from 2016 to 2021, Atmos. Chem. Phys., 22, 10919–10935, https://doi.org/10.5194/acp-22-10919-2022, 2022.

Teoh, R., Engberg, Z., Shapiro, M., Dray, L., and Stettler, M.: A high-resolution Global Aviation emissions Inventory based on ADS-B (GAIA) for 2019–2021, https://doi.org/10.5194/egusphere-2023-724, 1 June 2023.

Vignati, E., Wilson, J., and Stier, P.: M7: An efficient size-resolved aerosol microphysics module for large-scale aerosol transport models, Journal of Geophysical Research: Atmospheres, 109, https://doi.org/10.1029/2003JD004485, 2004.

Yu, F., Turco, R. P., and Kärcher, B.: The possible role of organics in the formation and evolution of ultrafine aircraft particles, J. Geophys. Res., 104, 4079–4087, https://doi.org/10.1029/1998JD200062, 1999.

Yu, F., Kärcher, B., and Anderson, B. E.: Revisiting Contrail Ice Formation: Impact of Primary Soot Particle Sizes and Contribution of Volatile Particles, Environ. Sci. Technol., 58, 17650–17660, https://doi.org/10.1021/acs.est.4c04340, 2024.

Zhang, K., O'Donnell, D., Kazil, J., Stier, P., Kinne, S., Lohmann, U., Ferrachat, S., Croft, B., Quaas, J., Wan, H., Rast, S., and Feichter, J.: The global aerosol-climate model ECHAM-HAM, version 2: sensitivity to improvements in process representations, Atmospheric Chemistry and Physics, 12, 8911–8949, https://doi.org/10.5194/acp-12-8911-2012, 2012.